Applied Thermal Engineering 273 (2025) 126491

Contents lists available at ScienceDirect

Applied Thermal Engineering

journal homepage: www.elsevier.com/locate/apthermeng

Research Paper

Investigation of the impact of the thermodynamic property method on the performance, preliminary component sizing and maximum efficiency configuration of the NET power cycle

Ivan Velazquez [a,*], Frederiek Demeyer [b], Miriam Reyes [a]

[a] Department of Energy and Fluid Mechanics Engineering, University of Valladolid, Paseo del Cauce 59, 47011 Valladolid, Spain
[b] Department of Mechanics & Thermal Processes, Engie R&I (Laborelec), Rodestraat 125, 1630 Linkebeek, Belgium

ARTICLE INFO

Keywords:
Oxy-combustion
NET power cycle
Supercritical CO_2 cycle
Equations of state
CO_2-capture

ABSTRACT

This paper investigates the effect of thermodynamic property methods on the NET Power cycle, which is a novel supercritical CO_2 power cycle based on the oxy-combustion technology. A numerical model of the most advanced configuration of NET Power cycle and air separation unit was developed in Aspen Plus to characterize the thermodynamic performance, key components presizing, and maximum efficiency operating configuration. The Peng-Robinson cubic Equation of State (EoS) has traditionally been adopted as the reference EoS (REF EoS) in previous thermodynamic studies on the NET Power cycle. However, its elevated predictive uncertainty, especially in phase modeling, may have led to inconsistent results. For that reason, and as a novelty, in present work, different EoS such as cubic, viral, SAFT and multiparametric Helmholtz free energy-based methods were considered, to evaluate the effect of the EoS on the cycle components and to optimize the operating conditions of the cycle. REFPROP + LKP was also included as the most reliable method. The results reveal that REFPROP + LKP estimates a fluid density in the liquid-like phase pumping stages 25 % higher than the cubic EoSs at nominal conditions. Thus, the compression work is 11.57 % lower and the net cycle efficiency 1.48 % higher. The higher relative deviations in cycle efficiency were obtained with PC-SAFT and GERG-2008 models. REF EoS estimates a recirculation pump impeller diameter 7.49 % larger than REFPROP + LKP. An oversized pump would operate outside the design point with low efficiency, flow control difficulties, and potential vibration and overpressure issues. For REFPROP + LKP, the heat exchange area required by the recuperator is 6.46 % lower than that estimated by REF EoS. This suggests that the manufacturing costs are significantly lower and transient response faster than expected. The maximum cycle efficiency resulted in 55.94 %, for a combustor outlet temperature of 1103.93 °C, turbine inlet and outlet pressures of 273.99 bar and 44.83 bar, and bypass split fraction of 11.37 %.

1. Introduction

Global primary energy consumption was 619.63 Exajoules in 2023, rising 1.4 % since 2013. However, total CO_2 emissions from energy augmented 0.7 % in this period [1,2]. With the aim of achieving the net zero emission targets by 2050, Carbon Capture & Storage Systems are expected to be key enablers [3]. Among the various CO_2 capture systems, oxy-combustion is a promising technology for emission-free energy production [4]. It consists of burning fuel with high purity oxygen at near stoichiometric conditions. The resulting combustion gases are mainly composed of CO_2, water, and a reduced impurity content. The steam is condensed and separated from the main stream, while the impurities are removed in a purification unit.

Based on oxy-combustion technology, several power cycle embodiments have been proposed, including the Semi-Closed Oxy-Combustion Combined Cycle, the MATIANT cycles, the NET Power Cycle, the Graz cycle, the CES cycle and the AZEP cycle. A complete revision of these cycles can be found in Mancuso et al. [5]. The net efficiency of the different cycles is in the range of 43.6–65 %, among which only the AZEP, CES and NET Power cycle can currently be considered in an advanced stage of development [6]. The NET Power cycle has the best average performance with the lowest total plant specific cost, 1560 €/kW [5]. Moreover, the NET Power cycle presents 5.6 % and 11.5 % higher efficiency than the Semi-Closed Oxy-Combustion Combined Cycle and MATIANT cycles, respectively [3–5].

The NET Power cycle analysis carried out by Mancuso et al. [5] was extended by Scaccabarozzi et al. [7] and Colleoni et al. [8] by analyzing

* Corresponding author.
E-mail address: ivan.velazquez@uva.es (I. Velazquez).

https://doi.org/10.1016/j.applthermaleng.2025.126491
Received 11 February 2025; Received in revised form 25 March 2025; Accepted 13 April 2025
Available online 15 April 2025

Nomenclature

A	heat transfer area [m^2]
c_p	specific heat at constant pressure [$kjkg^{-1}K^{-1}$]
D	representative magnitude of the turbomachine geometry [m]
d_s	specific diameter [m]
h	specific enthalpy [$kJkg^{-1}$]
K_1, K_2, K_3	calibration parameters
$\dot{m}$	mass flow rate [kgs^{-1}]
n_s	specific speed [$rads^{-1}$]
p	pressure [kPa]
$\dot{Q}$	heat flow rate [MW]
T	temperature [K]
U	overall heat transfer coefficient [$MWm^{-2}K^{-1}$]
$\dot{\mathscr{V}}$	volumetric flow rate [m^3s^{-1}]
$\dot{W}$	work flow [MW]
z	compressibility factor
ΔT_{lm}	log mean temperature difference [K]

Greek symbols

Ω	diameter of the distillation column [m]
β	volumetric expansivity [K^{-1}]
ρ	density [kgm^{-3}]
ω	rotational shaft speed [$rads^{-1}$]

Subscripts

C	coolant
c	cold-side of the recuperator
EXP	expander
H	mixer outlet
h	hot-side of the recuperator
I	expander inlet
O	expander outlet
Reb	reboiler
W	wall

Acronyms

ASU	air separation unit
BWRS	Benedict-Webb-Rubin-Starling
COT	combustor outlet temperature
CPA	cubic plus associating
EoS	equation of state
EOS-CG	equation of state of combustion gases
LHV	low heating value
LKP	Lee-Kesler-Plöcker
PC-SAFT	perturbed chain – statistical associating fluid theory
PR	Peng-Robinson
PSO	particle swarm optimization
RD	relative deviation
REF	Reference
RKS	Redlich Kwong Soave
SAFT	statistical associating fluid theory
sCO_2	supercritical CO_2
TIP	turbine inlet pressure
TOP	turbine outlet pressure
TPM	thermodynamic property method
VLE	vapor–liquid equilibrium

and optimizing the main operating parameters for maximum efficiency. Parametric analyses were conducted and a configuration with a maximum cycle efficiency of 54.8 % was obtained. Haseli et al. [9] integrated an air separation unit (ASU) model and analyzed the thermodynamic performance of the assembly, finding a 59.7 % of maximum cycle efficiency. From the ASU proposed by Allam et al. [10] and the NET Power cycle layout of Allam et al. [11], Mitchell et al. [12] incorporated a cryogenic liquid O_2 storage to improve the operational flexibility of the plant. When the O_2 demanded by the cycle is provided by a storage tank, temporary efficiencies of 66.1 % were reported. Other papers have proposed novel cycle layouts; Chan et al. [13] introduced an expansion with intermediate reheating, while Xie et al. [14] proposed an integrated cogeneration system consisting of a NET Power cycle and a heat pump that recovers CO_2 heat from the compression train, improving the efficiency of the original cycle by 1.56 %. Yu et al. [15] suggested the use of liquified natural gas, proposing strategies to use the cold energy of the liquified natural gas to cool the CO_2 in the compression train. Wang et al. [16] proposed a novel system to simultaneously generate power, methane and freshwater, with a NET Power cycle efficiently governing the assembly. An artificial neural network was trained to emulate the energy behavior of the system. A multi-objective optimization was conducted to maximize the freshwater mass flow, exergy efficiency, and cost rate, resulting in 378.5 kg/s, 39.03 %, and 11.021 $/h, respectively. Xie et al. [17] proposed a modification in the compression train of the NET Power cycle to produce freshwater and clean energy. Heat from compression is employed in an evaporative desalination system to produce freshwater. The efficiency of the system was 49.11 %, with a capacity to generate 292.64 kg/s of freshwater. Luo et al. [18] performed an exergy analysis of a coal-fired NET Power cycle, reporting an overall exergy efficiency of 40.6 %. Combining a coal-fired NET Power cycle with a coal gasification process, Zhao et al. [19] conducted a parametric study with the main process variables, resulting in a net efficiency of 38.87 %. More details on the status of the NET Power cycle research and development are provided in [20].

Accuracy in the assessment and modeling of the NET Power cycle performance depends deeply on the prediction of the thermodynamic properties of the working fluid from a thermodynamic property method (TPM). Therefore, it is crucial that the selected TPM can accurately compute properties such as specific volume, heat capacity and vapor–liquid equilibrium (VLE). For this purpose, it is important to note the working fluid of the NET Power cycle lies in the supercritical regime [21]. The NET Power cycle is represented in a pressure – specific enthalpy diagram for pure CO_2 on Fig. 1. Isocontours of the compressibility factor (z) and of the product of the volumetric expansivity (β) and temperature, βT, have also been included. z denotes the deviation of a real gas from ideal gas behavior. At elevated temperatures, the gas during expansion approaches ideal gas behavior ($z \approx 1$). However, as the fluid approaches the critical point, strong real gas effects occur in the fluid as is noticed by an abrupt decrease of z. The increase of βT in such a region leads to a deflection of the isotherm lines at lower enthalpy values as the pressure increases. These factors lead to the exhibition of strong variations in the thermo-physical properties of the fluid in the region near the critical point, with transitions between liquid-like and gas-like properties (gray and orange regions in Fig. 1). The higher the pressure, the lower the intensity of these property variations.

Although the real gas effects for pure CO_2 can be accurately predicted using the Span & Wagner model [22], uncertainties still exist when dealing with the impact of impurities (H_2O, CO, H_2, O_2, N_2, Ar and CH_4) on the volumetric and phase behavior of the CO_2 mixture. The presence of impurities in the pseudo-critical domain can significantly vary the properties of CO_2 in a highly non-ideal manner [23]. In most of the numerical studies on the NET Power cycle [5,7,12–15,18,19,24,25], the Peng-Robinson (PR) and Soave-Redlich-Kwong (SRK) cubic EoSs were adopted as TPMs. Specifically, the PR EoS with Van der Waals one fluid as mixing rule is the most widely employed for providing the best

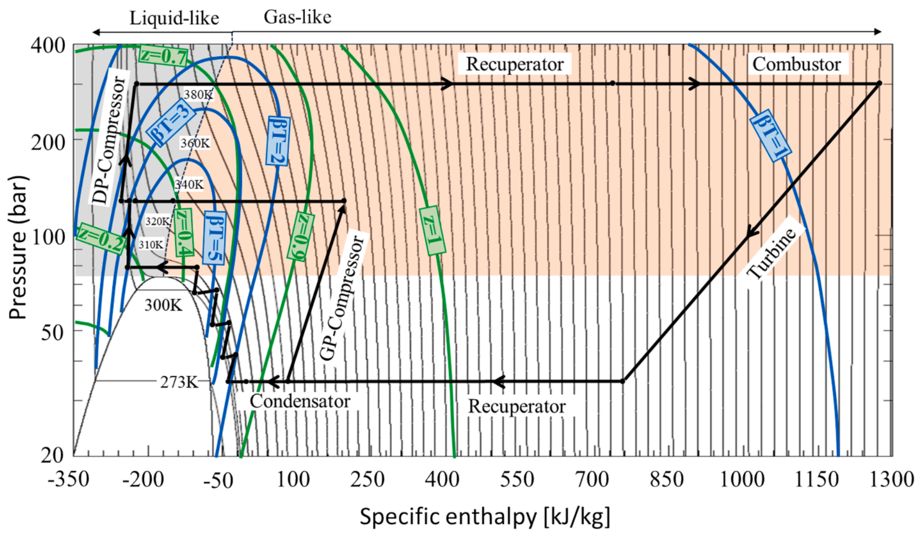

Fig. 1. Representation of the NET Power cycle in a pressure-specific enthalpy diagram for pure CO_2 (using the Span & Wagner EoS [22]) including lines of constant z and βT. DP stands for Dense-Phase and GP for Gas-Phase. Strong real gas effects appear close to the critical point.

balance between a low computational time and a reasonable accuracy in volumetric calculations [23]. This has led the authors to establish the PR EoS as the reference TPM for the NET Power cycle modeling. However, an in-depth study justifying whether the PR EoS leads to reliable predictions of the thermodynamic performance of the NET Power cycle was not addressed. To conduct this evaluation becomes necessary considering that, for phase and volumetric calculations, the interaction parameters significantly affect the accuracy of the PR EoS [26,27]. This is particularly true for the supercritical liquid-like phase. Thus, considering the simple mathematical formulation of the PR EoS, it is unfeasible to calibrate the interaction parameters for the whole pressure and temperature domain covered by the NET Power cycle working fluid. This implies that, in certain pressure and temperature regions, the predictive uncertainty becomes high. In addition to cubic EoSs, virial-type, Statistical Associating Fluid Theory (SAFT) type and multiparametric-type formulated in terms of the Helmholtz residual free energy, have been widely employed to model supercritical CO_2 (sCO_2)-rich mixtures.

Li et al. [27] compared the performance of cubic EoSs with virial-type, Benedict-Webb-Rubin-Starling (BWRS) and Lee-Kesler-Plöcker (LKP) EoS; SAFT type, Perturbed-Chain SAFT (PC-SAFT) EoS; and the multiparametric-type, GERG-2008; for the prediction of the density of CO_2-N_2, CO_2-O_2 and CO_2-Ar mixtures. The results pointed out a clear superiority of GERG-2008. Mazzoccoli et al. [28] selected for comparison a Cubic EoS (Advanced PR), the Cubic Plus Associating (CPA) and GERG-2008. VLE data for 20 different CO_2 mixtures and density data for 27 mixtures, in pressure ranges of 0–20 MPa and temperatures of 253.15–313.15 K were collected. GERG-2008 reported more accurate results for density and bubble point. With the aim of increasing the computational efficiency of the CPA EoS, Xiong et al. [29] presented a novel general cross-association explicit formulation for different bonding types. Accurately modeling the phase behavior of CO_2-rich systems, the new formulation resulted in a CPU time decrease of 70 %. The GERG-2008 model shows deficiencies regarding the description of the phase behavior of CO_2 mixtures, permanently underestimating the solubility of gases in the aqueous phase [30]. The development of the Equation of State for Combustion Gases (EOS-CG) in 2016 addresses these shortcomings. Gernert et al. [31] compared EoSs PR and SRK, PC-SAFT, CPA, GERG-2008 and EOS-CG for VLE and density of CO_2-H_2O mixtures. PR with the Huron-Vidal mixing rule and EOS-CG reported the best performance with an absolute averaged relative deviation of 4.5 % and 8 % for phase equilibrium, and 2.8 % and 0.6 % for density. EOS-CG presents the best performance in predicting the phase and volumetric behavior for CO_2-rich mixtures [32]. The EOS-CG model was recently updated and extended into a new model EOS-CG-2021 [33]. 72 binary mixture models were added, five departure functions and 14 binary mixture models with fitted reduced parameters were elaborated. McKay et al. [34] analyzed the capability of the PR, SRK, PC-SAFT, GERG-2008 and EOS-CG models to characterize CO_2-rich mixtures. Results revealed relative errors of the PR and SRK EoSs predicting the CO_2 solubility in H_2O of 88.6 % and 89.9 %, respectively. The PR EoS performs significantly better with the Huron-Vidal mixing rules, reporting an error of 3.5 %. GERG-2008 and EOS-CG reported an error of less than 1 % computing the density of multicomponent CO_2-rich systems over a temperature and pressure range of 273.15–423.15 K and 11–1260 bar. PR and SRK EoSs, with the Peneloux volume shift, reported deviations of 2.8 % and 4.8 % in the supercritical phase. SAFT models demonstrated similar performance to the cubic EoSs.

Several computational studies on various outdated NET Power cycle layouts have been conducted. The PR EoS was adopted as a reference TPM in the NET Power cycle literature for providing low computational cost. However, The PR EoS was chosen without a thorough study of the TPM influence on the NET Power cycle. A literature review reveals that the PR EoS can yield significant deficiencies in property predictions of sCO_2-rich mixtures within the supercritical regime, especially in the phase modeling. This could lead to inconsistent results. Furthermore, more advanced TPM formulations were developed to improve the predictions accuracy. Therefore, it is noticeable that a study elaborating on the influence of TPMs on the NET Power cycle is still required. For this reason, this paper presents as a novelty a comprehensive study on the influence of the TPMs on the thermodynamic performance, component sizing and maximum efficiency configuration of the NET Power cycle. Findings of this study will quantitatively explain the deviations incurred by previous studies. Furthermore, it will serve as a reference on TPMs for future research on the NET Power cycle. To this end, a thermodynamic model of the NET Power cycle and the ASU have been developed, along with a methodology to quantify the impact of the TPMs on the cycle components and to optimize the main operating parameters of the cycle. This work is based on the most advanced NET Power cycle configuration patented to date. Thus, the operating configuration for maximum efficiency is also presented as a novelty. The paper is divided into four sections; a detailed description of the NET Power cycle and ASU is presented in Section 2. The models and methodology implemented are described in Section 3, results are presented and discussed in Section 4, and finally, the main conclusions derived from the study are summarized in Section 5.

2. NET Power cycle description

In Fig. 2 is presented the process flow diagram of the NET Power cycle and the ASU. Natural gas (fuel) enters the pressurized combustion chamber together with an oxidizing stream (OX-3), which contains the necessary oxygen (diluted in CO_2 for safety reasons [18]) to carry out the combustion process with an excess oxygen percentage of 3 %. The high-pressure recirculation stream (RE-7), composed mainly of CO_2, acts as a combustion temperature moderator. The resulting flue gas (FG-1) is at a high temperature and pressure. These gases, together with a fraction of the pressurized recirculated CO_2 stream (TC-2), which serves as a turbine coolant, are expanded while producing mechanical work on the turbine shaft. The hot turbine exhaust gas (FG-2) is passed through a recuperative heat exchanger to partially preheat the recirculating streams, preferably cooling the exhaust gases to a temperature below the dew point of the mixture after leaving the recuperator. Exiting the recuperator (FG-3), a cooling step condenses and removes the water derived from the combustion. A fraction, equivalent to the CO_2 generated in the combustion, is then extracted from the cycle and conducted to a CO_2 capture unit. The recirculation gas (RE-1) is compressed in a multistage compressor with intermediate cooling. The compressor discharge pressure is set as a function of the ambient air and cooling tower conditions. This pressure is approximately 80 bar for a minimum cycle temperature of 26 °C [7,35]. In supercritical liquid-like phase, the recirculation stream RE-2 is compressed to 120 bar, which is the pressure of the high purity (99.5 % mol O_2) ASU-derived O_2 stream (O2-4). The stream RE-4 is then split into two streams: (i) RE-5, which contains the combustion temperature moderator and turbine coolant; (ii) the remaining flow is used as an O_2 diluent to form the oxidizer stream (OX-1) [11]. Both streams are compressed in dense phase to the upper cycle pressure of 300 bar and sent to the thermal recuperator to complete the cycle.

The favorable thermo-physical properties of the fluid near the critical point result in reduced compression work and thus high cycle efficiencies. However, the heat capacity of CO_2 on the high-pressure cold side of the recuperator is significantly higher than the one on the low-pressure hot side [36]. This limits the maximum temperature that the recycling streams can reach. To attenuate this undesired effect, the application of additive heating to the recuperator from additional thermal energy sources is used. According to Allam et al. [25], part of the compression thermal energy of the ASU air may be recovered. Following the same approach, a fraction of the exhaust gases can be adiabatically compressed to generate an additional heat input in the recuperator [11]. Then, the bypass stream BP-1 is extracted at a temperature above the dew point (138 °C is considered [11,12]) and adiabatically compressed up to 120 bar to be fed back into the recuperator. After leaving the recuperator (BP-3), the water is condensed and removed, and the resulting gas is recirculated together with the main stream. These improvements were implemented in the cycle modeling.

The ASU model considered in this study is based on the cryogenic air distillation system for high-pressure O_2 production [10]. The air separation method consists of a double distillation column system, with a lower part operating at a pressure of 5.4 bar (high pressure column) and an upper part operating at a pressure of 1.25 bar (low pressure column).

The inlet ambient air stream is compressed in the adiabatic main air compressor (MAC) to 5.6 bar. The thermal energy of the pressurized air

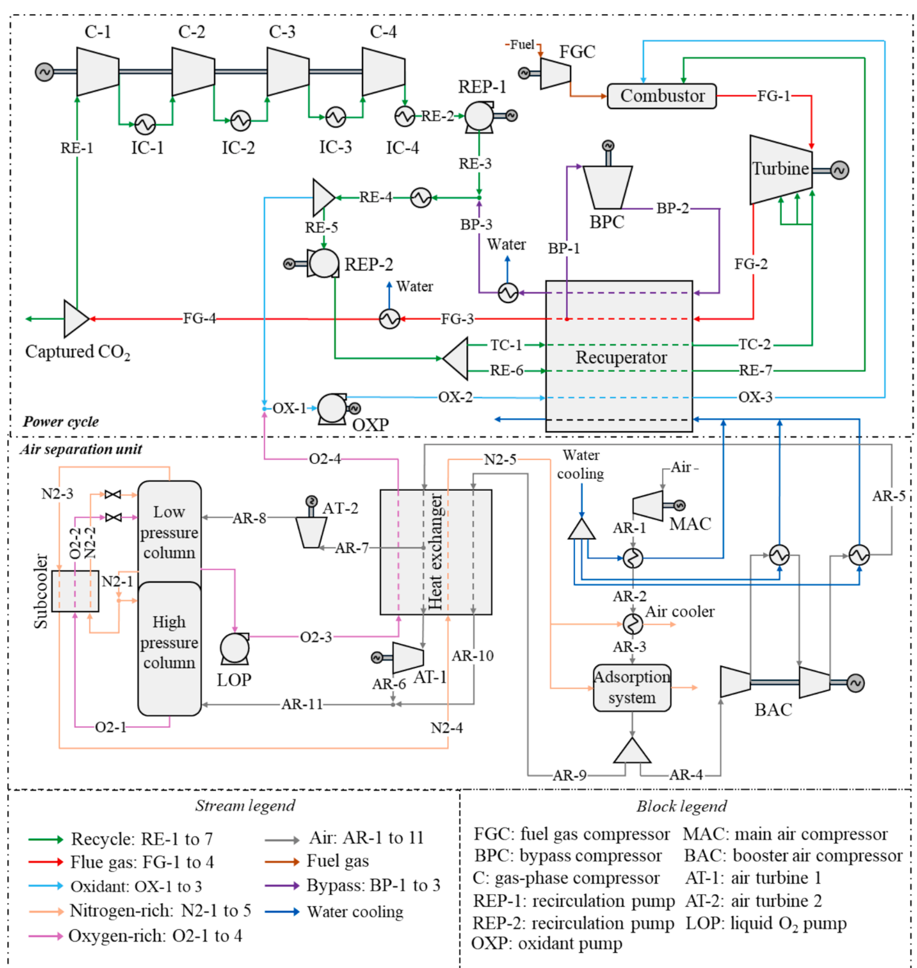

Fig. 2. Process flow diagram of the NET Power cycle and the cryogenic distillation separation unit. Stream and block legends were included.

(AR-1) is then utilized in the main recuperator of the power cycle, leaving the heat exchanger at a temperature of 54 °C (AR-2) [12]. The air is cooled again in the air cooler to 15 °C [12] from a chilled water stream (not shown) obtained by direct contact of an inlet cooling water stream with a portion of residual N_2. The pressurized cooled air (AR-3) enters the purification system where CO_2, H_2O, and hydrocarbon traces are removed [9]. The purification system is composed of adsorption beds regenerated with residual nitrogen. A portion of the purified air (30 % vol.), AR-4, enters a booster air compressor (BAC) to be compressed to 90 bar. The resulting high-pressure air stream (AR-5) is partially cooled in the main recuperative heat exchanger. A portion corresponding to 20 % vol. (AR-7) is expanded in an air turbine (AT-2) to a pressure of 1.25 bar and a temperature of approximately −189 °C [10], and then introduced into the middle section of the low pressure column. The remainder air is further cooled in the heat exchanger to −101 °C [10] and expanded in the turbine AT-1 to a pressure of 5.4 bar (AR-6). As for the main air stream, AR-9, it is cooled in the heat exchanger and joined with AR-6, so that the resulting stream feeds the lower part of the high pressure column (AR-11) at its saturation temperature (−174 °C) with a vapor fraction of 77 % [10]. The liquid N_2 stream (N2-1) formed in the boiler/condenser is used as reflux for the high pressure and low pressure columns. Both the former and the O_2-enriched liquid stream obtained from the bottom of the high pressure column (O2-2 and N2-2) are subcooled below their respective saturation temperatures against the residual N_2 leaving the top of the low pressure column. The resulting streams, prior to feeding the low pressure column, are expanded at constant enthalpy by valves up to the low pressure column operating pressure. N2-2 is introduced at the top and O2-2 is introduced in the same section as AR-8. The high-purity liquid O_2 stream leaving the low pressure column as a product at the bottom, is pumped up to 120 bar and used as a cold stream along with the residual N_2 in the heat exchanger.

3. Methodology, models and assumptions

The methodology used to estimate the impact of the chosen TPM on the thermodynamic performance of the NET Power cycle, the preliminary sizing of the components and the maximum efficiency operating parameters is presented in this section.

3.1. Selected thermodynamic property methods

Eight TPMs were selected for the comparison analysis: two Cubic EoS, PR and SRK; two Virial-type EoS, LKP and BWRS; two SAFT-type EoS, PC-SAFT and CPA; and the multiparametric GERG-2008 EoS. The interaction coefficients of the PR, SRK, LKP, BWRS, PC-SAFT and CPA EoS used in this study are shown in Table 1. These interaction coefficients were adjusted by Velazquez et al. [37].

The PR EoS, with the default binary interaction parameters provided by Aspen Plus [38], was taken as the reference for being the most employed in the NET Power cycle literature. Hence, this EoS will be referred to as REF EoS in the following. On the other hand, the calibrated PR, SRK, LKP, BWRS, PC-SAFT and CPA EoSs, as well as the GERG-2008 EoS, will be referenced as the TPMs in the following. In addition, [37] reported the following conclusions: (i) the NIST REFPROP [39] is the TPM that most accurately predicts the density of sCO_2-rich mixtures and (ii) the calibrated LKP EoSs is the model that best calculates the equilibrium phase composition for the CO_2-H_2O system. The former being crucial to properly model the heat transfer process in the low temperature section of the NET Power cycle thermal recuperator. Accordingly, an additional comparison will be performed between the results derived by the REF EoS, and those using REFPROP to calculate the fluid density and LKP to predict the phases composition within the recuperative heat exchanger. Special attention will be paid to this comparison in the results section. Comparisons between TPMs will be quantified using the Relative Deviation (RD), which is defined for a generic thermodynamic index ϕ as follows:

$$RD[\%] = \frac{\phi_{TPM} - \phi_{REF}}{\phi_{REF}} \bullet 100. \tag{1}$$

3.2. NET Power cycle and ASU modeling and assumptions

The NET Power cycle and ASU have been integrated and developed in the commercial process simulation software Aspen Plus V12.1 [38], which contains the TPMs selected in Section 2.1. Some authors modeled the NET Power cycle in different process simulation softwares such as gPROMS Process Builder, IPSEpro or Engineering Equation Solver. However, the versatility of Aspen Plus has made it the most widely used process modeling package in the academic and industrial fields. Thus, in an effort to maximize the spread of the outcomes derived from this research, Aspen Plus was the chosen platform.

Models are based on the diagrams detailed in section 2. The recirculation flow RE-1 (see Fig. 2) is adjusted to keep the combustor outlet temperature constant at 1150 °C under the assumption of constant fuel thermal input. The O_2-diluting portion of the CO_2 stream is adjusted so that the mole fraction of O_2 in the OX-1 stream is 13.34 % [7]. The input data and model assumptions are given in Table 2. The models of the process components (turbines, compressors, pumps, heat exchanger, …) have been taken directly from the blocks available in Aspen Plus. The ASU cryogenic distillation columns have been modeled using the RadFrac block. A more detailed modeling for the cooled turbine and thermal recuperator has been conducted due to their complexity. Details of the modeling are presented in this section.

3.2.1. sCO_2 turbine model

The cooled expansion model must provide the following features: (i)

Table 1
Calibrated interaction coefficients of the PR, SRK, LKP, BWRS, PC-SAFT and CPA EoSs based on experimental density and VLE data of sCO_2-rich binary mixtures [37].

		CO_2-H_2O		CO_2-CO	CO_2-H_2	CO_2-O_2	CO_2-N_2	CO_2-Ar	CO_2-CH_4
		VLE	ρ	ρ	ρ	ρ	ρ	ρ	ρ
PR	$k_{ij}^{(1)}$	−0.4274	−0.0823492	0.0000	0.0000	−0.144269	0.0000	−0.128005	−0.229886
	$k_{ij}^{(2)}$	0.001	0.00130716	−0.00085152	−0.002656	0.00094759	−0.00109974	0.0000	−0.00093592
SRK	$k_{ij}^{(1)}$	−0.4614	0.0000	0.0000	0.0000	0.0603179	0.0000	−0.189057	0.0000
	$k_{ij}^{(2)}$	0.0011	−0.0010648	0.00149822	−0.021956	0.0000	−0.00087398	0.0000	−0.0789253
LKP	k_{ij}	0.0125	−0.278075	0.114011	0.916455	0.0253371	0.0901669	0.0200776	−0.489781
BWRS	k_{ij}	0.1053	0.0000	−0.181284	−0.681987	0.0130965	−0.476755	−0.033787	0.0531
PC-SAFT	$a_{i\alpha,j\beta}$	0.1565	0.0929834	−0.999539	−0.284113	0.205097	−0.96324	0.0000	0.0000
	$b_{i\alpha,j\beta}$	0.1449	0.116352	0.959316	−0.999873	−0.256288	0.996573	0.0732153	0.99997
	$e_{i\alpha,j\beta}$	0.0228	−0.0494549	−0.0147781	0.0000	0.0000	−0.576246	0.0000	0.998752
CPA	$k_{ij}^{(1)}$	0.168	0.285987	−0.211483	0.0000	0.503948	0.567561	0.0000	−0.412014
	$k_{ij}^{(2)}$	0.269	0.241135	−0.207193	0.0000	−0.455381	−0.011355	−0.037751	0.0000

Table 2
Input parameters and assumptions for the NET Power cycle and ASU models developed in Aspen Plus.

Parameter	Unit	Value
Net Power cycle		
Fuel low heating value (89 % CH_4, 7 % C_2H_6, 1 % C_3H_8, 0.1 % C_4H_{10}, 0.01 % C_5H_{12}, 2 % CO_2, 0.89 % N_2, [% vol])	MJ/kg	46.502
Fuel temperature and pressure	°C/bar	15/70
Percentage of O_2 excess in combustion	%	3
O_2 mole fraction in the oxidizer stream	%	13.34
Minimum cycle temperature	°C	26
Bypass stream output temperature	°C	138
CO_2 gas-phase compressors isentropic efficiency	%	85
Fuel gas compressor isentropic efficiency	%	85
SCO_2 dense-phase pumps hydraulic efficiency	%	85
Turbine stages isentropic efficiency	%	89
Mechanical efficiency of all turbomachinery	%	98
Recuperator high-pressure flows pressure drop	%	0.66
Recuperator low-pressure flows pressure drop	%	2.94
Combustor pressure drop	%	1
Condenser and intercoolers pressure drop	%	2
Air Separation Unit		
Ambient air temperature, pressure and relative humidity	°C/bar/%	15/1.013/60
O_2 purity	% (mol)	99.5
O_2 temperature and pressure	°C/bar	18/120
Air compressors isentropic efficiency	%	85
Air turbines isentropic efficiency	%	85
O_2 pump hydraulic efficiency	%	80
Intercoolers pressure drop	%	1
High pressure column stages	–	45
Feed air inlet stage to the high pressure column (starting from the top)	–	45
High pressure column reflux ratio (molar basis)	–	1.2
Low pressure column stages	–	69
N_2-enriched stream inlet stage to the low pressure column	–	1
O_2-enriched stream inlet stage to the low pressure column	–	28
Feed air inlet stage to the low pressure column	–	28
Low pressure column reflux ratio (molas basis)	–	0.516

the ability to incorporate TPMs that reproduce the behavior of real gas mixtures; (ii) rely exclusively on several calibration parameters and not require turbine geometrical information. Haseli et al. [9] used the model adapted from [40] to determine the coolant mass flow, while other authors, [5,7,12,14,19], adopted the continuous expansion model proposed by El-Masri [41] and adapted by Scaccabarozzi et al. [7].

In the El-Masri model, the expansion process is divided into *N + 1* stages. The first *N* stages correspond to the cooled section of the turbine (see Fig. 3), and the last expansion step (*N +* 1) represents the adiabatic section of the turbine. Each cooled expansion step is composed of an adiabatic expander, *EXP-I*; a mixer, *MIX-i*, mixing the coolant flow *Ci* associated with *EXP-i* with the main stream *Oi*; and a valve (*VALVE-i*). The isentropic efficiency of all expanders is assumed to be the same. The first *N* expanders have the same pressure ratio, which is iteratively adjusted to obtain $T_{I,N} = T_W$, where T_W is the maximum allowable material temperature, 860 °C. The pressure ratio of the adiabatic expansion section (*N +* 1) is automatically established to obtain the defined turbine outlet pressure. The number of turbine cooling stages *N* has been fixed at 11 since, according to Zhao et al. [19], a larger number of stages does not imply large differences in the total coolant flow calculation, although significantly increase the computational cost. The mass flow of each coolant stream, $\dot{m}_{Ci}$, is calculated from the following expression:

$$\dot{m}_{Ci} = K_1 \frac{T_{Ii} - T_W}{T_W - T_{Ci}} \dot{W}_{EXP-i}, \tag{2}$$

where K_1 is a calibration parameter representing the turbine geometry and operating conditions, T_{Ii} is the inlet temperature of the *EXP-I*, T_{Ci} is the inlet temperature of the coolant and $\dot{W}_{EXP-i}$ is the power delivered by the expander *i*. The pressure drop caused by the addition of refrigerant, $p_{Oi} - p_{Ii+1}$, is calculated according to the following correlation:

$$p_{Oi} - p_{Ii+1} = K_2 \left(\frac{\dot{m}_{Ci}}{\dot{\mathscr{V}}_{Hi}} \right)^{K_3}, \tag{3}$$

where K_2 and K_3, like K_1, are calibration parameters and $\dot{\mathscr{V}}_{Hi}$ is the volumetric flow rate at the *VALVE-i* inlet. The parameters K_1, K_2 and K_3 were taken directly from [7].

3.2.2. Recuperator

The heat transfer process in the recuperator is deeply conditioned by the strong variations experienced by the thermo-physical properties of the fluid near the critical point [8]. Moreover, the addition of additive heating to the recuperator at different temperatures and the water condensation led to the occurrence of multiple pinch-points. To model the recuperator, Allam et al. [11] employed three heat exchangers in series: two multi-stream, corresponding to the low- and medium temperature sections and another two-stream for the high-temperature section. Similarly, Mitchell et al. [12] and Colleoni et al. [8] used the approach of [11] but dividing the high temperature exchanger into two, so that the turbine coolant is extracted in the intermediate section. They further discretized the resulting layout into a finite number of heat transfer stages to account for the non-linear variation of the heat capacities of the blended CO_2 streams. Excluding the additive heating by the bypass compressor, Scaccabarozzi et al. [7] and Chan et al. [13] divided the recuperator into two multi-stream heat exchangers, and Wimmer et al. [42] into three.

In this study, the recuperator has been modeled using a single multi-stream heat exchanger [43] discretized into 100 heat exchange stages. The outlet temperatures of the CO_2 recirculation stream and the oxidizing stream have been set equal and obtained from the constraint of maintaining an internal pinch-point of 5 °C. The pinch-point can occur on the cold side of the recuperator or at the dew point of the turbine exhaust gases. The *Complex* optimization algorithm (available in Aspen Plus V12.1) adjusts the turbine coolant outlet temperature to maximize the outlet temperature of the recycling streams, while the hot-side temperature approach must be greater than or equal to 10 °C. The bypass stream temperature at the recuperator extraction has been set to 138 °C [11]. The outlet temperature of the hot streams are equal and derived from the energy balance within the heat exchanger.

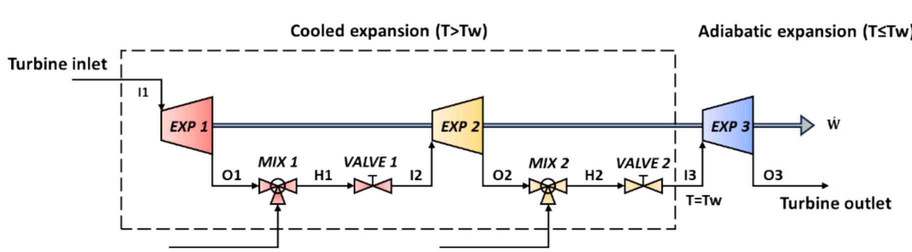

Fig. 3. Diagram of the adapted El-Masri refrigerated expansion model for two cooled expansion stages (N = 2). Mixers and valves model the cooling and pressure drop caused by the coolant injection.

3.3. Methodology for preliminary component design

The pre-design of the thermal recuperator is characterized by the product of the overall heat transfer coefficient (U) and the heat exchange area (A), UA. The sizing of the turbomachines is defined by a magnitude representative of the geometry D (i.e., the impeller diameter of a radial flow machine or the ratio between the length and the chord of a blade in an axial flow turbomachine). The diameter Ω sizes the distillation columns. All simulations concerning the impact on the components pre-design have been conducted under the nominal operating conditions shown in Table 3.

3.3.1. Heat exchangers

The coefficient UA is a beneficial form to characterize the performance and size of a heat exchanger. The UA parameter can be obtained from the transferred heat flow rate $\dot{Q}$ and the log mean temperature difference ΔT_{lm}, which are process variables obtained from cycle simulation:

$$UA = \frac{\dot{Q}}{\Delta T_{lm}} = \frac{\dot{Q}}{\frac{\Delta T_c - \Delta T_h}{\ln(\Delta T_c/\Delta T_h)}}. \tag{4}$$

In Eq. (4) ΔT_c and ΔT_h are the temperature differences on the cold- and hot-side of the heat exchanger, respectively [44].

3.3.2. Turbomachinery

The similarity parameters specific speed (n_s) and specific diameter (d_s), defined in Eqs. (5) and (6) have been used for the pre-design of the turbomachines [35,36].

$$n_s = \frac{\omega\sqrt{\dot{\mathscr{V}}}}{(\Delta h)^{3/4}} \tag{5}$$

$$d_s = \frac{D(\Delta h)^{1/4}}{\sqrt{\dot{\mathscr{V}}}} \tag{6}$$

ω is the angular shaft speed, Δh is the isentropic change of specific enthalpy, D is a representative geometric magnitude of the turbomachine (characteristic length). $\dot{\mathscr{V}}$ is the volumetric flow rate at the inlet or outlet of the turbomachine depending on whether it is a compressor or a turbine, respectively [45,46]. $\dot{\mathscr{V}}$ is estimated from the mass flow and the fluid density calculated by the TPM. ω was fixed such that n_s equals 1 for the REF EoS [47]. Therefore, for each chosen TPM, n_s is first determined by Eq. (5). Then, d_s is estimated from a $n_s - d_s$ Balje diagram, which was fitted by polynomials in Eq. (7) by Du et al. [48]. Finally, D is obtained by Eq. (6). To quantify the impact on the turbomachine sizing of the TPM choice, the relative deviation (expressed in Eq. (1)) in the prediction of D between the REF EoS and the rest of TPMs has been used.

$$\log_{10} d_s = \begin{cases} -0.6433x + 0.7068, x < -0.79 \\ 0.4890 - 0.4264x + 0.6387x^2 - 0.6370x^3 \\ -0.2498x^4 + 0.3800x^5 - 0.1965x^6, -0.79 < x < 1.4 \\ 0.0764, x > 1.4 \end{cases}, \tag{7}$$

with $x = \log_{10} n_s$..

3.3.3. Distillation columns

The impact on the distillation columns sizing has been quantified from the relative deviation of the calculated diameter Ω between the REF EoS and the rest of TPMs. Ω can be obtained from the volumetric flow rate of gas rising through the column $\dot{\mathscr{V}}_{reb}$ (process variable calculated in the ASU model) according to the following expression [49]:

$$\Omega = 0.87\,\dot{\mathscr{V}}_{reb}^{\;0.5} \tag{8}$$

3.4. Numerical process optimization methodology

The numerical optimization problem has been handled with the black-box approach. That is, the simulation model in Aspen Plus is considered as a black-box function, so that the direct search optimization method programmed in MATLAB [50] generates the decision variable set and sends it to the Aspen Plus black-box function through an ActiveX server. Then, Aspen Plus computes the cycle performance and sends it back to the MATLAB optimizer.

The objective function to be maximized is the net cycle efficiency. The decision variables, as well as their bounds and the (non-linear) design constraints are shown in Table 4. The output of the process simulation model is non-smooth and presents noise [7]. Therefore, a hybrid derivative-free numerical optimization algorithm suitable to deal with this kind of objective functions has been implemented in MATLAB. The optimization method is composed of two algorithms (whose solutions are shared) corresponding to a global search process, particle swarm optimization (*PSO*); and a local search step, *Complex* algorithm modified by [51]. First, the algorithm generates an initial population of random decision variables satisfying the design constraints [52]. Then, at each iteration, the algorithm executes the following two steps: (i) a global search consisting of an update (iteration) of the current set of decision variables according to the *PSO* algorithm; (ii) if the global search step fails to find a better value of the objective function, a local search consisting of two reflections is performed according to the *Complex* algorithm. If the global search step was successful, step (ii) is skipped. A population size of 50 and a complex of 12 vertices (twice the number of decision variables) has been set. The set of decision variables that form the vertices of the complex are those closest to the global optimum in each iteration.

Non-linear design constraints and hidden constraints, which come

Table 3
NET Power cycle base (nominal) operating conditions.

Parameter	Unit	Value
Thermal energy of feedstock (LHV)	MW_{th}	768.19
Combustor outlet temperature	°C	1150
Turbine Inlet Pressure	bar	300
Turbine Outlet Pressure	bar	34
Bypass stream Split fraction	%	6
Recuperator hot-side temperature approach	°C	10
Recuperator pinch-point	°C	5
Minimum fluid temperature	°C	26
Multi-stage intercooled compressor outlet pressure	bar	80
Intermediate sCO_2 pump outlet pressure	bar	120

Table 4
Objective function, decision variables and (non-linear) design constraints involved in the numerical optimization process of the NET Power cycle.

	Parameters	Bounds
Objective function	Net cycle efficiency	–
Independent decision variables	Recycle stream mass flow rate (which controls the combustor outlet temperature)	600 – 1800 [kg/s]
	Turbine inlet pressure	200–400 [bar]
	Turbine outlet pressure	20–60 [bar]
	Recuperator outlet temperature of the recycle and oxidant streams	500–840 [°C]
	Recuperator outlet temperature of the turbine coolant flow	50–600 [°C]
	Bypass stream split fraction	0–15 [%]
Design (non-linear) constraints	Hot side temperature approach of the recuperator	≥ 10 [°C]
	Pinch-point of the recuperator	≥ 5 [°C]

from a numerical convergence failure of the process simulation software, are handled with a penalty function. That is, if any constraint is violated the objective function is set to infinity. The stopping criteria has been set to 500 total iterations of the algorithm (steps i and ii). Because of the *meta*-heuristic nature of the optimization method, the algorithm was executed five times with each TPM to reach global optimum solutions.

3.5. Model validation

The performance of the numerical model developed in this work was validated against previous results obtained by Mitchel et al. [12] and Scaccabarozzi et al. [7]. Mitchel at al. incorporated the bypass recompression loop and an ASU model. In contrast, Scaccabarozzi et al. did not consider the bypass loop and assumed that the ASU energy penalty is 1391 kJ/kgO$_2$. Including in the validation process two data sources from slightly different cycle embodiments increases the reliability of the results derived in this study. The comparison of results was performed under the same cycle operating conditions as Scaccabarozzi et al., shown in Table 5. Moreover, the same EoS, PR EoS, was employed.

Table 6 presents the comparison of the major output variables with previous studies. The turbine output power was slightly higher in the Mitchel et al. study, as a result of a different expansion model than used in the rest of works. The inclusion of the bypass compressor leads to a higher CO_2 compression power for this work compared to Scaccabarozzi et al. The ASU energy penalty resulted similar in all studies. This ensures credible results from the ASU model developed in this study. The net cycle efficiency predicted in this work had a relative error of −1.56 % versus that estimated by Scaccabarozzi et al. The most significant difference between the Mitchel et al. study and this study compared to Scaccabarozzi et al. was the turbine coolant temperature. The additional compression heat supplied to the recuperator by the bypass compressor justifies the temperatures of 435.55 °C and 511.7 °C against 182 °C. The similarity between the results ensures the applicability and reliability of the model developed for this study.

4. Results and discussions

The results of the impact of the TPM used for the calculation of the NET Power cycle working fluid properties are discussed in this section. The calibrated PR, SRK, LKP, BWRS, PC-SAFT and CPA EoSs, as well as the GERG-2008 EoS and the combination of REFPROP + LKP, are referred as TPMs. The PR EoS, with the default binary interaction coefficients provided by Aspen Plus, is referred to as the REF EoS. As REFPROP + LKP is the most reliable TPM evaluated in this study, special consideration is given to the comparison between REFPROP + LKP and REF EoS. Streams and components of the NET Power cycle are referenced with the abbreviations of the process diagram of Fig. 2.

4.1. Impact of the chosen TPM on the thermodynamic performance of the NET Power cycle

4.1.1. General trends at nominal conditions

The thermodynamic performance of the NET Power cycle at nominal conditions of Table 3, as a function of the chosen TPM, is presented in Table 7. In addition, in Fig. 4 the relative deviations in the prediction of the fluid density at the suction of the compressors and pumps are represented.

Table 5
Key parameters for model validation.

Key parameter	Unit	Value
Combustor outlet temperature	°C	1150
Turbine inlet pressure	bar	300
Turbine outlet pressure	Bar	34
Recuperator hot side ΔT	°C	20
Recuperator pinch-point ΔT	°C	5
Minimum fluid temperature	°C	26

Table 6
Comparison of results with previous studies under the operating conditions shown in Table 5.

Output variable	Unit	This work	Mitchel et al. [12]	Scaccabarozzi et al. [7]
Fuel thermal input	MW$_{th}$	768.31	768.31	768.31
Turbine power output	MW$_e$	623.01	673.20	622.42
CO_2 compression	MW$_e$	121.98	126.71	111.15
Fuel compression	MW$_e$	4.26	4.29	4.18
ASU consumption	MW$_e$	81.08	83.30	85.54
Auxiliary penalties	MW$_e$	2.85	13.45	2.24
Net power output	MW$_e$	412.84	445.40	419.31
Net cycle efficiency	%	53.73	57.97	54.58
Turbine inlet mass flow	kg/s	1252.92	1203.00	1271.0
Turbine coolant mass flow	kg/s	157.207	190.30	99.40
Turbine coolant temperature	°C	435.55	511.70	182.00

All TPMs predict a similar turbine power output of 625 MWe, since the behavior of the high temperature gas during expansion is close to the ideal gas behavior. The power consumption of the gas compressors estimated by the TPMs is higher than that estimated by the REF EoS. This is because the fluid density in the compressors estimated by the TPMs is lower than that by the REF EoS, as shown in Fig. 4. In the suction of the REP-1 and REP-2 pumps, the TPMs predict a fluid density notably higher than REF EoS. It can be seen in Fig. 4 that the PR and SRK cubic EoSs underestimate the density more than the other TPMs. Ibrahim et al. [53] also observed that the SRK EoS significantly underestimates the density of the CO_2-H_2O system at supercritical conditions. As the pumping specific work is inversely proportional to the fluid density, the power consumed by REP-1 and REP-2 is lower than that calculated by REF EoS. This leads to a total reduction of −11.57 % in the pumping power consumption for REFPROP + LKP. As a result, the net cycle efficiency is higher than predicted by REF EoS. In particular, REFPROP + LKP predicts a net cycle efficiency 1.48 % higher than REF EoS. PR and LKP reported a different behavior, computing a similar density as the REF EoS for the sCO_2 pumps, while underestimating the density of the oxidizing mixture by −25 %. Considering REFPROP + LKP as the most reliable TPM in Aspen Plus, these findings suggest that the liquid-like pumping stages are not being adequately modeled in the NET Power cycle literature.

Fig. 5 represents the relative deviation in the prediction of the hot composite curve within the thermal recuperator. The exhaust gases leaving the recuperator, FG-3, are at a lower temperature than estimated by the REF EoS. This is because the fluid density in the REP-1 and REP-2 is higher than predicted by the REF EoS, as shown in Fig. 4. Thus, the fluid heating by viscous dissipation during compression diminishes and the CO_2 recirculation streams, RE-6 and TC-1, enter the recuperator at a lower temperature. As a result, for REFPROP + LKP, the exhaust gas temperature at the recuperator outlet is 10.62 % lower than for REF EoS. This leads to a noticeable reduction in the cooling energy demanded by the water separator. The discontinuities that appear in Fig. 5 are produced by the heat capacity flow (product of the mass flow and the specific heat at constant pressure $\dot{m}c_p$) change at the dew point, which coincides with the pinch-point of the recuperator, and by the addition of hot air from the ASU.

Since the hot streams leave the recuperator at a lower temperature than estimated by the REF EoS, more heat is delivered by them. In addition, cold streams require more energy to reach the target hot-side temperature approach of 10 °C, since these streams are introduced into the recuperator at a lower temperature. However, two effects occur that

Table 7
Thermodynamic performance of the NET Power cycle at the base cycle conditions shown in Table 3. Values of the thermodynamic indexes are only provided for the REF EoS, and the relative deviations for the rest of TPMs according to Eq. (1).

	REF (PR)	PR [%]*	SRK [%]	LKP [%]	BWRS [%]	PC-SAFT [%]	CPA [%]	GERG-2008 [%]	REFPROP +LKP [%]
Thermodynamic performance indexes									
Thermal energy of feedstock (LHV) [MW_{th}]	*768.19*	0.00	0.00	0.00	0.00	0.00	0.00	0.00	0.00
Turbine power output [MW_e]	*624.84*	0.42	1.16	0.09	0.54	1.26	0.28	0.52	0.26
Gas-phase compressor train consumption [MW_e]	*55.14*	0.45	2.59	1.20	4.16	5.60	5.40	2.96	2.60
Dense-phase pumps consumption [MW_e]	*54.34*	0.50	−1.72	−1.27	0.95	−8.03	−10.71	−11.86	−11.57
Bypass compressor consumption [MW_e]	*12.03*	0.45	1.99	0.18	9.97	2.25	1.49	1.53	1.26
Fuel gas compressor consumption [MW_e]	*4.26*	−0.71	5.15	3.19	3.15	1.05	3.27	2.68	2.67
ASU consumption [MW_e]	*81.09*	0.00	0.00	0.00	0.17	0.00	0.00	0.00	0.00
Net cycle efficiency [%]	*54.41*	0.49	1.50	0.11	−0.21	2.11	1.03	1.86	1.48
Main dependent parameters									
Turbine outlet temperature [°C]	*737.95*	−0.03	0.28	−0.61	−0.48	−1.16	0.14	−0.76	−0.59
Flue gas to condenser temperature [°C]	*62.90*	−2.58	−0.52	−4.64	21.34	−15.92	−11.94	−12.82	−10.62
Turbine coolant temperature [°C]	*208.74*	33.89	14.25	5.63	85.39	113.15	−23.59	65.97	50.15
Turbine coolant flow rate [kg/s]	*106.65*	11.98	6.74	0.46	33.62	50.35	−6.29	23.35	16.46
Turbine inlet flow rate [kg/s]	*1290.58*	−0.33	0.06	−0.41	0.71	−1.54	0.46	−0.70	−0.47

***[%] = relative deviation** $= \frac{\Phi_{TPM} - \Phi_{REF}}{\Phi_{REF}} \bullet 100$

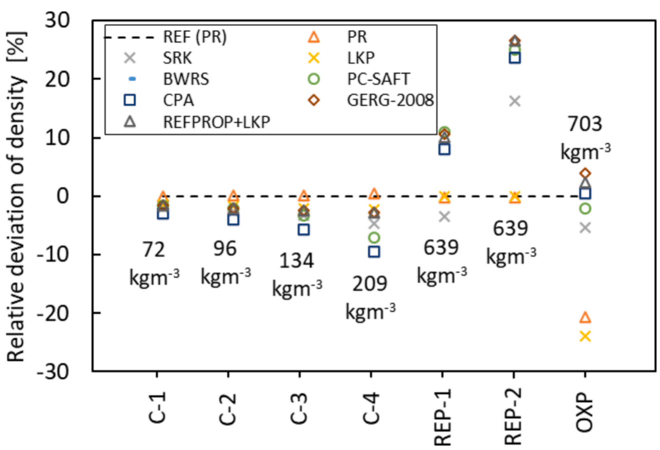

Fig. 4. Relative deviation in the calculation of the fluid density at the inlet of the four compression stages and pumps. The numerical density values were obtained with the REF EoS. The BWRS EoS has relative deviations lower than −30 %. Density is overestimated by the REF EoS in the compressor and underestimated by up to 25 % in the REP-1 and REP-2 pumps.

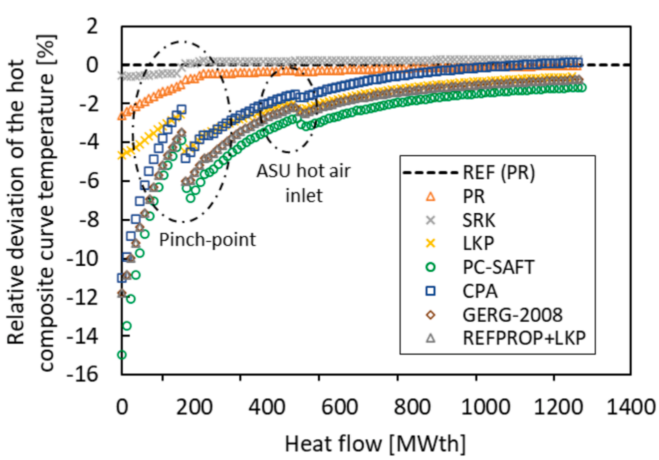

Fig. 5. Relative deviation in the calculation of the temperature of the hot composite curve within the thermal recuperator. TPMs predict an exhaust gas temperature leaving the recuperator significantly lower than REF EoS.

produce an excess of available heat in the recuperator for TPMs in comparison to the REF EoS: (i) the hot streams will deliver more latent heat of condensation as gradually cooled below the dew point, and (ii) the inlet temperature of the recirculation streams is further below the pseudocritical temperature (i.e., the temperature at which c_p reaches the maximum value). This means that the heat capacity of the cold streams is lower in the low-temperature section of the recuperator. Then, the temperature change of the cold streams in the recuperator is higher than predicted by the REF EoS. This leads to an overall increase in the recuperator effectiveness. This excess of available heat causes an augment of the turbine coolant temperature leaving the recuperator, as deduced from Table 7. This results in a turbine coolant mass flow rise according to Eq. (2). The higher the turbine coolant temperature, the higher the expansion power. However, the increase in coolant flow causes a higher circulative flow performing a thermodynamic cycle of lower maximum temperature, which results in a decrease in the overall efficiency. The excess of available heat was not estimated by most previous studies on the NET Power cycle that employed the REF EoS. Thus, this finding suggests that the recuperator design conditions should be updated to leverage the heat excess. For example, reducing the hot-side temperature approach and the fraction of exhaust gas by the bypass compressor, would improve the recuperator effectiveness.

4.1.2. Efficiency trends as a function of the combustor outlet temperature, turbine inlet pressure and turbine outlet pressure

The NET Power cycle efficiency as a function of the combustor outlet temperature (COT), turbine inlet pressure (TIP) and turbine outlet pressure (TOP), is shown in Fig. 6 for each TPM considered. A comparison between the REF EoS and REFPROP + LKP, including the actual efficiency values is presented in Fig. 6a, 6c and 6e., and the relative deviations of all TPMs with respect to the REF EoS are presented in Fig. 6b, 6d and 6f. COT has been varied between 1050 °C and 1300 °C, by adjusting the recirculation mass flow; TIP between 240 bar and 340 bar; and TOP between 28 bar and 48 bar. The rest of parameters have been kept constant and equal to those specified in Table 3. In general, TPMs predict higher efficiency for all COT, TIP and TOP ranges compared to the REF EoS because of the lower estimated compression work of the sCO_2 pumps. As can be noticed from Fig. 6, the maximum efficiency deviations were reported by PC-SAFT, which resulted in 2.81 % for COT of 1050 °C, 2.61 % for TIP of 340 bar and 2.37 % for TOP of 48 bar. LKP and BWRS notably underestimate the fluid density in the supercritical regime, which explains their different trend from the rest of TPMs.

REFPROP + LKP calculates a higher density of the recirculation streams in the pumping, as shown in Fig. 4. This leads to a reduction of

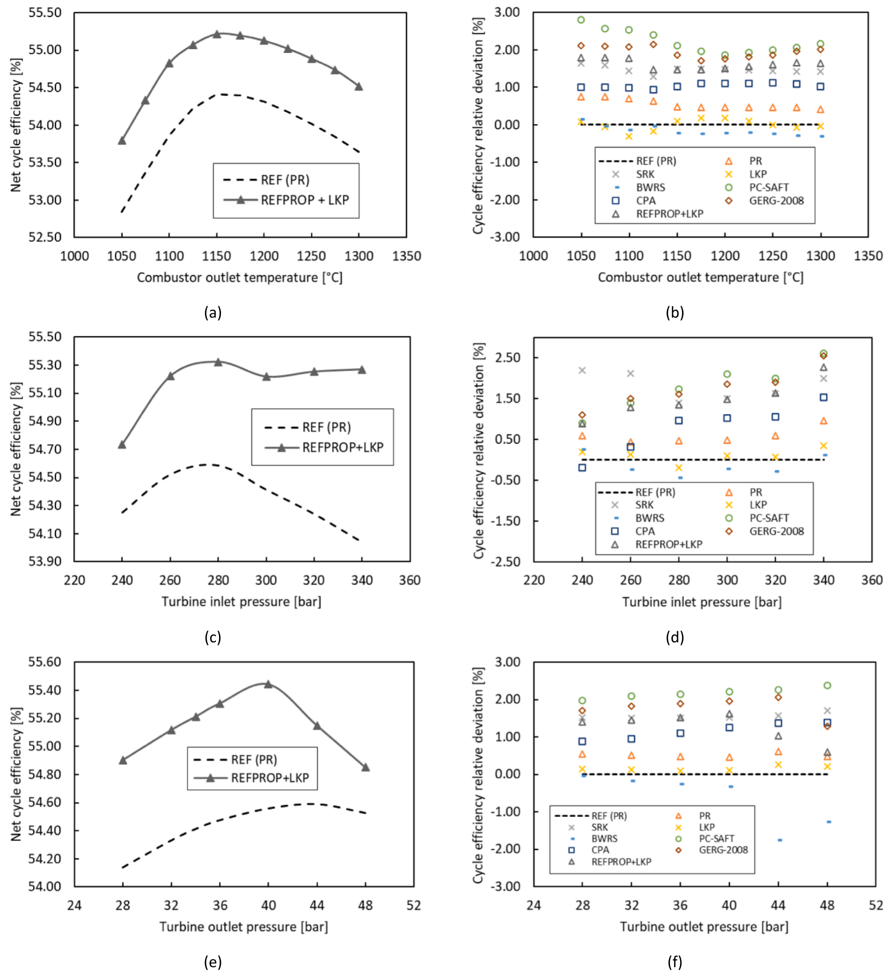

Fig. 6. NET Power cycle efficiency for REF EoS and REFPROP + LKP, and the efficiency relative deviation for all TPMs with respect to the REF EoS as a function of COT (a and b), TIP (c and d), and TOP (e and f). TPMs estimate cycle efficiencies up to 3 % higher than REF EoS in the COT, TIP and TOP ranges of 1000–1350 °C, 220–360 bar, and 24–52 bar, respectively.

the pumping work and a cycle efficiency between 1 and 3 % higher than REF EoS over the entire COT range. The efficiency trend is similar, exhibiting a peak at 1150 °C. For REFPROP + LKP, the efficiency peak value is 55.22 %, and for REF EoS it is 54.41 %. Above this temperature, the energy excess from the exhaust gases overheats the turbine coolant, deteriorating the efficiency. With the rest of TPMs, an efficiency of 0.5 – 3 % higher than that for the REF EoS is obtained, as depicted in Fig. 6b. Below 1150 °C, the exhaust gases do not have enough thermal energy to preheat the recirculation streams up to the hot-side temperature specification of the recuperator. Thus, the efficiency decays. The excess of available heat in the recuperator predicted by the PR, PC-SAFT, GERG-2008 and REFPROP + LKP EoSs results in the recirculation streams leaving the recuperator at a higher temperature than expected by the REF EoS. This justifies the slight increase on the efficiency difference obtained by TPMs with respect to the REF EoS below 1150 °C shown in Fig. 6b.

The efficiency calculated with REFPROP + LKP is between 0.5 – 2.5 % higher than for the REF EoS over the entire TIP range considered, with a maximum efficiency at 280 bar, as shown in Fig. 6c. Below 280 bar, the efficiency decreases due to three factors: (i) the net power decay due to the lower advantage obtained from the low compression work of the sCO_2 pumps. (ii) The overheating of the turbine coolant due to the increase of the exhaust gases thermal energy. (iii) The increment of the heat capacity of the recirculation streams within the recuperator due to its approach to the critical point, which promotes the high temperature heat exchange and exergy destruction. An efficiency of up to 3 % higher for the TPMs with respect to the REF EoS is observed in Fig. 6d. Also, the higher the TIP, the higher the efficiency relative deviation. This fact is noticed in Fig. 6c, where above 280 bar the efficiency for REFPROP + LKP remains approximately constant instead of decaying, as occurs for the REF EoS. This efficiency drop for the REF EoS is because as TIP increases, the thermal energy of the exhaust gases decreases. Thus, the recirculation streams leave the recuperator at a lower temperature and the total flow through the cycle is reduced to maintain COT at 1150 °C. For PR, SRK, PC-SAFT, CPA, GERG-2008 and REFPROP + LKP, the net power is higher than for the REF EoS as TIP increases because: (i) the compression work of the sCO_2 pumps is lower, and (ii) the excess of available heat in the recuperator produces an increase in the turbine coolant flow and a minor reduction in the total flow.

As can be seen in Fig. 6e, the efficiency calculated with REFPROP + LKP is between 0.5 and 2.5 % higher than for the REF EoS over the entire TOP considered. However, the evolution of the efficiency as a function of TOP presents differences. For REF EoS, a maximum efficiency is found at a TOP of 44 bar, decreasing smoothly beyond this pressure. For REFPROP + LKP, the efficiency peak occurs at 40 bar. Below 40 bar, the efficiency decays smoothly with a similar slope as presented by the REF EoS. However, the efficiency drop becomes abrupt for pressures above 40 bar. This is because the fluid enters the vapor–liquid region at the suction of the last gas compression stage (C-4) for a minimum cycle temperature of 26 °C. Consequently, the fluid temperature should be increased to ensure that the mixture is at least in the saturated vapor state for the proper compressor operation. This results in an increase in the fluid specific volume and an increment of the compression work. As shown in Fig. 1, compressor operation is close to the mixture dew point. Hence, using a TPM with high uncertainty predicting saturation conditions of sCO_2-rich mixture (such as REF EoS [34]) can drive the compressor to an operation within the biphasic region. This leads to a significant reduction of its lifetime. Okoro et al. [54] studied the effect of CH_4, O_2, Ar and N_2 on the saturation properties of CO_2-rich binary mixtures for temperatures between 228.15 – 273.15 K. They found that the presence of non-condensables, even at mole fractions as low as 0.5 %, increase the risk of biphasic flow in CO_2-rich systems at high pressure. The rest of TPMs predict an efficiency up to 2.5 % higher than for the REF EoS, as deduced from Fig. 6f.

4.2. Impact of the chosen TPM on the preliminary sizing of the main components of the NET Power cycle

4.2.1. Turbomachinery

Fig. 7 shows the relative deviation in the calculation of the characteristic length of the compressors and pumps (Fig. 7a), and turbine (Fig. 7b), as a function of the chosen TPM with respect to the REF EoS. On the *x*-axis the turbomachine is denoted by the abbreviations of the process diagram of Fig. 2. In Fig. 7.b, the eleven expanders forming the cooled turbine are shown (based on the El-Masri model described in Section 2.2.1).

TPMs predict a larger characteristic length for the four gas-phase compression stages. The deviation increases progressively for each compression stage as the fluid approaches the critical point. TPMs predict a lower fluid density during compression (as depicted in Fig. 4), which leads to an increment of the volumetric flow and specific work. This results in a larger compressor. The maximum relative deviation in the characteristic length of the fourth compression stage, produced by the CPA EoS, is 3.49 %. REFPROP + LKP reports only 1.19 %. Therefore, it can be concluded that the compressor design is roughly insensitive to the TPM. Thus, for compressor modeling and design purposes, cubic EoSs are recommended as they demand less CPU time.

Regarding the REP-1 and REP-2 pumps, the higher density predicted by the TPMs results in a lower volumetric flow and enthalpy change with respect to the REF EoS. Hence, the specific velocity increases and the specific diameter decreases, according to Eqs. (5) and (7). The decrease in volumetric flow and specific diameter causes a general reduction of the pumps size, as shown in Fig. 7a. Assuming that the characteristic length represents the impeller diameter, REFPROP + LKP predicts an impeller diameter for the REP-2 pump 7.49 % smaller than predicted by the REF EoS. This implies that a REP-2 design performed with the most widely used TPM in the NET Power cycle field, REF EoS, would result in a significantly oversized pump. This would have major practical implications for pump operation. An oversized pump would operate outside the design point, at conditions of lower efficiency than projected. Also, achieving accurate flow control would become more challenging, which can deviate the combustion process from stoichiometric conditions and diminish the overall efficiency of the cycle. Vibration and noise issues, including potential overpressures in the downstream equipment, could appear [55]. CPA, GERG-2008 and REFPROP, which are the most accurate models considered in this study, agree in estimating a REP-2 characteristic length of about −7.49 %. Specifically, CPA and GERG-2008 estimated a reduction of −7.06 % and −7.19 %, respectively. Thus, a design of the recirculation pumps should be conducted with the aforementioned TPMs.

Concerning the OXP, the density of the oxidizing mixture estimated by the TPMs is similar to the density predicted by the REF EoS (except for PR and LKP). Thus, the volumetric flow and pump head are similar. This results in a similar pump size. However, the underestimation of the fluid density by the PR and LKP EoSs with respect to the REF EoS implies that the volumetric flow is higher and the pump size increases. The BPC compresses the mixture from the minimum cycle pressure up to 120 bar. The fluid at these discharge conditions is in supercritical phase. However, fluid departs from the critical temperature and the compressibility factor value approaches the unity due to the temperature increase during compression. Therefore, the TPMs compute a value of the characteristic length for the BPC similar to that predicted by the REF EoS. The compressibility factor of the gas in the expansion process is close to unity, as a result of the elevated temperature. This implies that the gas behaves as an ideal gas, which means that the deficiencies of the TPMs predicting the fluid properties become negligible. This result in the turbine pre-sizing not being appreciably affected by the TPM, as deduced from Fig. 7b. For modeling and design intents of the OXP, BPC and turbine, the REF EoS can be used with negligible deviations.

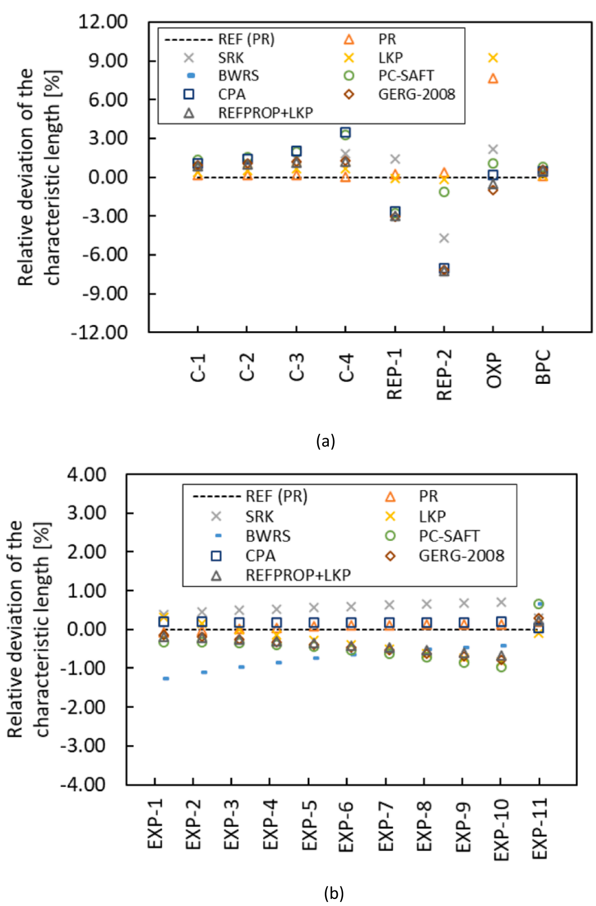

Fig. 7. Relative deviation in the calculation of the characteristic length of (a) the compressors and pumps, and (b) the expanders of the cooled turbine. The REP-2 pump is notably influenced by the TPM, with REFPROP + LKP predicting a 7.49 % smaller characteristic length. Turbine is not significantly influenced by the TPM.

4.2.2. Heat exchanger

Table 8 shows the relative deviation in the calculation of the transferred heat flow $\dot{Q}$, the log mean temperature difference ΔT_{lm}, and the UA product of the thermal recuperator as a function of the TPM. The TPMs predict a higher heat flow compared with the REF EoS (except for LKP and BWRS). This is due to the excess of available heat, as discussed in Section 4.1.1. TPMs compute a larger log mean temperature difference than REF EoS (except for CPA). With REFPROP + LKP, the log mean temperature difference is 8.08 % higher than for REF EoS. This results in a lower UA value than estimated by the REF EoS, as can be seen in Table 8. In the NET Power cycle recuperator, the heat transfer rate of the low-density exhaust gases is significantly lower than that of the high-pressure recirculating flows. Then, it can be assumed that the overall

Table 8
Relative deviation (RD) in the heat flow, log mean temperature difference and UA product of the thermal recuperator of the NET Power cycle as a function of the TPM. TPMs predict a higher log mean temperature difference than REF EoS, resulting in a significantly lower UA value.

	REF (PR)	PR	SRK	LKP	BWRS	PC-SAFT	CPA	GERG-2008	REFPROP + LKP
$RD(\dot{Q})$	0.00	0.84	0.99	−0.30	−1.13	1.95	0.98	1.28	1.09
$RD(\Delta T_{lm})$	0.00	5.18	3.69	3.34	15.11	1.90	−5.05	8.87	8.08
$RD(UA)$	0.00	−4.12	−2.60	−3.52	−14.11	0.05	6.35	−6.97	−6.46

heat transfer coefficient U becomes similar to the individual heat transfer coefficient of the hot gases. TPMs accurately predict the physical properties of the hot gases for having a pressure significantly lower than the critical pressure. Thus, it can be assumed that all TPMs predict a similar U value. This results in that, for REFPROP + LKP, the heat exchange area is 6.46 % less than that predicted by REF EoS. It is also important to note that the recuperator exchanges a heat flow of about 1.2 GW at nominal conditions [7], requiring a huge heat exchange area. Therefore, this finding has important practical consequences. A reduction in the amount of material reduces the manufacturing costs. This is especially transcendent for the high temperature heat exchange section, which is built from costly exotic nickel-based superalloys [56,57]. Regarding the operation of the recuperator, a reduction of the total mass accelerates the transient response to operating point changes, start-ups and shutdowns. This means that, in general, the competing potential of the NET Power cycle has been underestimated in the literature. Therefore, particular emphasis should be given to the TPM used for modeling and design purposes of the recuperator, recommending the use of REFPROP + LKP.

To explain the notable relative deviations in the log mean temperature differences, that cause the deviations in the UA product, Fig. 8 represents the evolutions of the heat capacity flows as a function of the temperature for the hot and cold composite curves. As depicted in Fig. 8, the evolution of the heat capacity flow for the cold composite curve is only presented for REFPROP + LKP and the REF EoS in benefit of the explanation. The heat capacity flow was calculated as the inverse of the composite curves slope. In Fig. 8a it can be seen three changes in the slope of the heat capacity flow for the hot composite curve: at approximately 112 °C, 138 °C, and 275 °C; corresponding to the exhaust gases dew point, the bypass gas extraction, and the hot air intake from the ASU. The TPMs compute an evolution of the heat capacity flow for the hot composite curve similar to the REF EoS, including the abrupt slope changes, since real gas effects are not relevant at the exhaust gas pressure. However, as deduced from Fig. 8b, the prediction of the heat capacity flow evolution for the cold composite curve by REFPOP + LKP presents discrepancies with respect to REF EoS. For REFPROP + LKP, the turbine coolant is extracted from the recuperator at a higher temperature, 313.42 °C, than predicted by the REF EoS, 208.75 °C due to the excess of available heat. This implies that the heat capacity flow drops (because of the extraction) at different temperatures. The decrease in the heat capacity flow causes an increase in the cold composite curve slope. Fig. 9 shows the evolution of the hot and cold composite curves between 50 and 500 °C. At low temperatures, the cold composite curves predicted by the REF EoS and REFPROP + LKP are close and evolve with a similar slope. When reaching 208.75 °C, the cold composite curve slope for the REF EoS increases. However, the cold composite curve slope for REFPROP + LKP does not increase until a higher temperature, 313.42 °C, is achieved. As a result, there is a larger separation between the cold composite curve and the hot composite curve for REFPROP + LKP than for the REF EoS. This justifies that the recuperator operated with a larger temperature difference for REFPROP + LKP than for the REF EoS.

4.2.3. Distillation columns

The relative deviations in the calculation of the volumetric flow rate $\dot{\mathscr{V}}$ and diameter Ω of the low pressure column and high pressure column

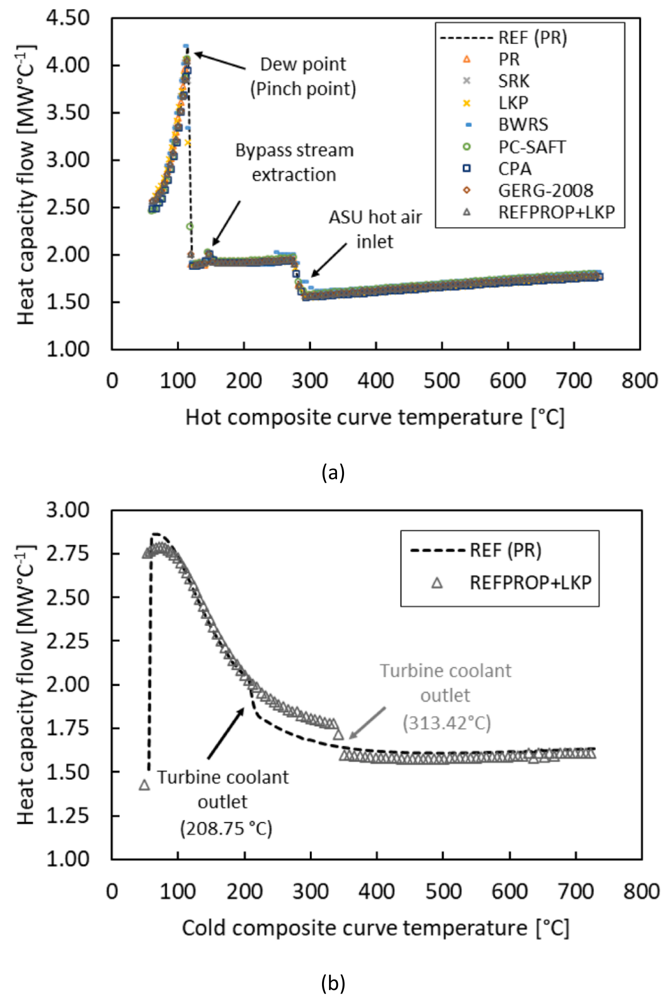

Fig. 8. Heat capacity flow evolution of (a) the hot composite curve for all TPMs, and (b) of the cold composite curve for the REF EoS and REFPROP + LKP. The heat capacity flow of the cold composite curve drops at a higher temperature (313.42 °C) for REFPROP + LKP.

are presented in Table 9. Deviations do not exceed 2 % (except for SRK), which means that the TPM employed does not substantially influence the ASU design. The discrepancies found for SRK lies in its periodic inaccuracy in predicting the partition coefficients in the vapor–liquid mixtures within the low-pressure distillation column.

4.3. Impact of the chosen thermodynamic method on the maximum efficiency operation points of the NET Power cycle

The thermodynamic performances of the NET Power cycle for the base case, and the maximum efficiency operating parameters for the REF EoS and REFPROP + LKP, are compared in Table 10. The results for the rest of the TPMs are shown in the Appendix A. The turbine inlet pressure value of maximum efficiency for REFPROP + LKP, 273.99 bar, is higher than that for the REF EoS, 265.74 bar. This is because the dense-phase

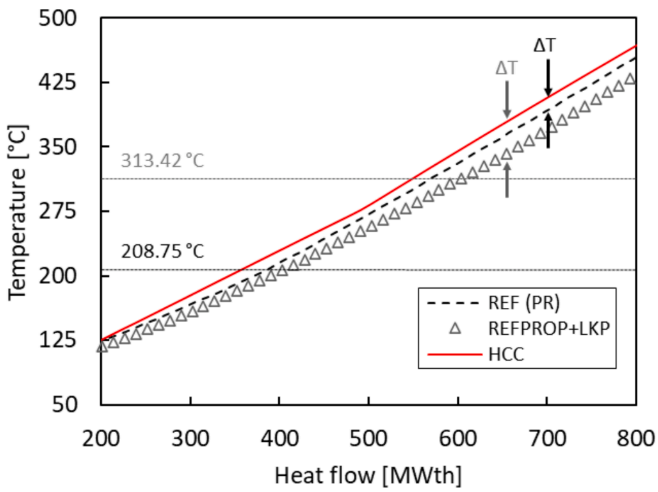

Fig. 9. Hot composite curve (in red) and cold composite curve (in black) for REF EoS and REFPROP + LKP. The heat capacity flow of the cold composite curve changes at higher temperature for REFPROP + LKP, which leads to a further separation of the composite curves.

compression work estimated by REFPROP + LKP is lower. In addition, for both REF EoS and REFPROP + LKP, the turbine inlet pressure for maximum efficiency is significantly lower than the base case, 300 bar. This finding is relevant regarding the turbine design. A lower turbine inlet pressure causes a reduction of the mechanical stresses in the blades and a potential savings in the design. The turbine outlet pressure for maximum efficiency for the REF EoS and REFPROP + LKP results significantly higher than for the base case. The subsequent augment of the thermal energy of the exhaust gases, which is recovered in the recuperator, compensates for the reduction in power output due to the lower turbine pressure ratio. This demonstrates that, maximizing the effectiveness of the recuperator, is key to maximizing the efficiency. This conclusion also serves to justify the increase in the bypass stream split fraction to 13.59 % and 11.37 %, for REF EoS and REFPROP + LKP, with respect to the base case value, 6 %. Then, the temperature of the recycle and oxidant streams leaving the recuperator increases, as shown in Table 10. As a result, the mass flow through the cycle is higher, with a value of 1410.67 kg/s for REFPROP + LKP. The maximum efficiency calculated with REFPROP + LKP, 55.94 %, is higher than that predicted by the REF EoS, 55.12 %, due to the lower power consumption. The fraction of exhaust gases fed into the bypass compressor is higher for the REF EoS and REFPROP + LKP than for the base case in benefit of the energy integration. This also promotes heat transfer in the low/medium temperature sections of the recuperator and reduces the exergy destruction.

5. Conclusions

The cubic Peng-Robinson EoS, with unadjusted interaction parameters, has traditionally been adopted as the reference EoS (REF EoS) to compute the thermophysical properties of the sCO_2-rich mixtures of the NET Power cycle. However, its predictive deficiencies, compared to more accurate TPMs, might lead to inconsistent outcomes. In this paper, a comprehensive investigation of the influence of TPMs on the NET Power cycle performance was presented. Thermodynamic behavior, turbomachinery and thermal recuperator presizing, and maximum efficiency operating configuration were evaluated. The TPMs PR, SRK, LKP, BWRS, PC-SAFT, CPA, GERG-2008, and the combination REFPROP + LKP were considered. The study was conducted based on a numerical model of the most advanced NET Power cycle and air separation unit embodiments developed in Aspen Plus. It has been found that uncertainties from TPMs result in significant differences in the prediction of the thermodynamic behavior of the NET Power cycle. The key findings of this research are as follows:

- Cubic EoSs underestimate the density of the sCO_2-rich mixture during liquid-like pumping by up to 25 % with respect to the most reliable TPM considered, REFPROP + LKP. Thus, REFRPOP + LKP estimates 11.57 % less pumping work. As a result, the net cycle efficiency is 1.48 % higher than that predicted by REF EoS at nominal conditions. The relative deviations in cycle efficiency for the remaining TPMs are: PR 0.49 %, SRK 1.50 %, LKP 0.11 %, BWRS −0.21 %, PC-SAFT 2.11 %, CPA 1.03 %, and GERG-2008 1.86 %. Because REFPROP + LKP considers a higher fluid density, the fluid heating by viscous dissipation during compression decreases. Therefore, stream temperatures on the cold-side of the recuperator decrease and the operative effectiveness of the recuperator rises. In general, TPMs predict efficiencies between 0.5 and 2.5 % higher than REF EoS for the COT, TIP and TOP ranges of 1050–1300 °C, 240–340 bar, and 28–48 bar, respectively.
- The sizing of the main compressor, bypass compressor and turbine are not significantly influenced by the TPM. Thus, for modeling and design purposes of the former turbomachines, it is recommended to use cubic EoSs since they demand less CPU time. Differences in the sizing of recirculation pumps as a function of the TPM were found.

Table 10
Maximum efficiency operating parameters for the REF EoS and REFPROP + LKP.

	Base case	REF (PR)	REFPROP + LKP
Turbine inlet pressure [bar]	300	265.74	273.99
Turbine outlet pressure [bar]	34	43.47	44.83
Total recycle flow rate [kg/s]	1319.23	1386.85	1410.67
Recuperator outlet temperature of recycle and oxidant streams [°C]	727.96	757.03	755.23
Recuperator outlet temperature of turbine coolant [°C]	208.74	227.46	242.40
Bypass stream split fraction [%]	6.00	13.59	11.37
Thermal energy of feedstock (LHV) [MW_{th}]	768.19	768.19	768.19
Turbine power output [MW_e]	624.84	627.12	622.25
Power consumption [MW_e]	206.86	203.73	192.50
Net cycle efficiency [%]	54.41	55.12	55.94
Turbine pressure ratio (TIP/TOP)	8.82	6.11	6.11
Combustor outlet temperature [°C]	1150	1100.70	1103.93
Turbine outlet temperature [°C]	737.95	767.03	765.32
Turbine coolant flow rate [kg/s]	106.65	96.80	98.94

Table 9
Relative deviation (RD) in the calculation of volumetric flow rates and diameters of the high and low pressure columns as a function of the TPM. The ASU is not significantly influenced by the TPM, unless SRK is used.

	REF(PR)	SRK	LKP	BWRS	PC-SAFT	CPA	GERG-2008	REFPROP + LKP
$RD\left(\dot{\mathscr{V}}_{LPC}\right)$	0.00	33.80	−2.18	−2.19	−0.06	−3.52	−1.55	−1.55
$RD(\Omega_{LPC})$	0.00	15.67	−1.09	−1.10	−0.03	−1.78	−0.78	−0.78
$RD\left(\dot{\mathscr{V}}_{HPC}\right)$	0.00	27.97	−0.76	−0.57	−0.82	−0.16	−0.59	−0.59
$RD(\Omega_{HPC})$	0.00	13.12	−0.38	−0.28	−0.41	−0.08	−0.30	−0.30

REFPROP + LKP predicts a REP-2 pump impeller diameter 7.49 % smaller than REF EoS. This means that a REP-2 design conducted by the REF EoS would lead to an oversized pump. This would result in a pump operating outside the design point with lower efficiency than projected, difficulties with accurate flow control, and potential vibrations and overpressures. Consequently, CPA, GERG-2008 or REFPROP + LKP should be employed to model recirculation pumps.
- For REFPROP + LKP the heat exchange area required by the recuperator is 6.46 % less than REF EoS. This is due to an accentuated separation of the composite curves within the recuperator, caused by the extraction of the turbine coolant at a higher temperature. A reduction in the amount of material significantly reduces manufacturing costs, considering the costly nickel-based superalloys involved. Moreover, the transient response is accelerated. REFPROP + LKP should be use to model and design the recuperator of the cycle.
- The optimization process results in a maximum cycle efficiency of 55.94 % for REFPROP + LKP. This is a result of decreasing the TIP from 300 bar to 273.99 bar, increasing the TOP from 34 bar to 44.83 bar, and increasing the bypass split fraction from 6 % to 11.37 %. This finding reveals that the recuperator is the key element of the cycle, as maximizing its effectiveness leads to maximizing the cycle efficiency.

Future research could focus on extending the present study to off-design conditions, updating the component models for partial loads, and including a larger number of TPMs. This would provide a more global perspective of cycle behavior.

Declaration of competing interest

The authors declare that they have no known competing financial interests or personal relationships that could have appeared to influence the work reported in this paper.

Acknowledgements

The authors acknowledge the University of Valladolid, Spain, for funding this research work. The authors would also like to acknowledge the entities Engie, Tree Energy Solutions (TES-H2), and the research group in Thermal Engines and Renewable Energies (MyER) from the University of Valladolid, for the technical contribution provided during the realization of this research work.

Appendix A. Maximum cycle efficiency operating parameters

Table A1
Maximum cycle efficiency operating parameters and thermodynamic performance indexes.

	PR	SRK	LKP	BWRS	PC-SAFT	CPA	GERG-2008
Turbine inlet pressure [bar]	206.01	300.27	260.01	284.6	297.96	284.83	291.87
Turbine outlet pressure [bar]	40.38	43.19	38.81	48.96	46.12	44.04	44.96
Total recycle flow rate [kg/s]	1406.44	1319.90	1337.36	1464.73	1393.14	1323.26	1330.88
Recuperator outlet temperature of recycle and oxidant streams [°C]	755.72	746.47	743.31	762.5	743.34	756.70	744.49
Recuperator outlet temperature of turbine coolant [°C]	262.8	123.99	293.73	284.6	322.34	312.33	382.71
Bypass stream split fraction [%]	9.47	11.12	12.86	11.85	10.23	14.99	14.99
Thermal energy of feedstock (LHV) [MW_{th}]	768.19	768.19	768.19	768.19	768.19	768.19	768.19
Turbine power output [MW_e]	625.46	630.26	630.83	619.8406	625.19	630.93	629.84
Power consumption [MW_e]	200.45	202.01	208.27	189.9782	193.87	202.42	198.95
Net cycle efficiency [%]	55.33	55.75	55.01	55.96	56.15	55.78	56.09
Turbine pressure ratio (TIP/TOP)	6.44	6.95	6.70	5.82	6.46	6.47	6.49
Combustor outlet temperature [°C]	1112.7	1113.20	1107.86	1099.76	1103.02	1115.99	1104.46
Turbine outlet temperature [°C]	765.73	756.47	753.31	772.56	754.17	766.70	754.49
Turbine coolant flow rate [kg/s]	107.51	86.37	107.06	105.96	109.27	119.93	123.94

Data availability

Data will be made available on request.

References

[1] Energy institute, Statistical Review of World Energy. 73rd edition, 2024.
[2] G. Aydin, H. Jang, E. Topal, Energy consumption modeling using artificial neural networks: The case of the world's highest consumers, Energy Sources Part B 11 (2016) 212–219, https://doi.org/10.1080/15567249.2015.1075086.
[3] IPCC, 2023: Climate Change 2023: Synthesis Report. Contribution of Working Groups I, II and III to the Sixth Assessment Report of the Intergovernmental Panel on Climate Change, Core Writing Team, H. Lee and J. Romero (eds.). IPCC, Geneva, Switzerland., 2023. https://doi.org/10.59327/IPCC/AR6-9789291691647.
[4] D.Y.C. Leung, G. Caramanna, M.M. Maroto-Valer, An overview of current status of carbon dioxide capture and storage technologies, Renew. Sustain. Energy Rev. 39 (2014) 426–443, https://doi.org/10.1016/j.rser.2014.07.093.
[5] L. Mancuso, N. Ferrar, P. Chiesa, E. Martelli, M. Romano, Oxy-combustion Turbine Power Plants, 2015. www.ieaghg.org.
[6] F. Climent Barba, G. Martínez-Denegri Sánchez, B. Soler Seguí, H. Gohari Darabkhani, E.J. Anthony, A technical evaluation, performance analysis and risk assessment of multiple novel oxy-turbine power cycles with complete CO2 capture, J. Clean Prod. 133 (2016) 971–985, https://doi.org/10.1016/j.jclepro.2016.05.189.
[7] R. Scaccabarozzi, M. Gatti, E. Martelli, Thermodynamic analysis and numerical optimization of the NET Power oxy-combustion cycle, Appl. Energy 178 (2016) 505–526, https://doi.org/10.1016/j.apenergy.2016.06.060.
[8] L. Colleoni, A. Sindoni, S. Ravelli, Comprehensive thermodynamic evaluation of the natural gas-fired allam cycle at full load, Energies (Basel) 16 (2023) 2597, https://doi.org/10.3390/en16062597.
[9] Y. Haseli, N.S. Sifat, Performance modeling of Allam cycle integrated with a cryogenic air separation process, Comput. Chem. Eng. 148 (2021) 107263, https://doi.org/10.1016/j.compchemeng.2021.107263.
[10] R.J. Allam, Cryogenic Air Separation Method for Producing Oxygen at High Pressures, United States Patent Application 20180073804 15 March 2018, n.d.
[11] R.J. Allam, B.A. Forrest, J.E. Fetvedt, Method and System for Power Production With Improved Efficiency. United States Patent Application 20180073434, pp. 15 March 2018, n.d.
[12] C. Mitchell, V. Avagyan, H. Chalmers, M. Lucquiaud, An initial assessment of the value of Allam Cycle power plants with liquid oxygen storage in future GB electricity system, Int. J. Greenhouse Gas Control 87 (2019) 1–18, https://doi.org/10.1016/j.ijggc.2019.04.020.

[13] W. Chan, X. Lei, F. Chang, H. Li, Thermodynamic analysis and optimization of Allam cycle with a reheating configuration, Energy Convers. Manag. 224 (2020) 113382, https://doi.org/10.1016/j.enconman.2020.113382.
[14] M. Xie, S. Liu, L. Chen, Y. Zhang, Y. Wang, S. Xie, Y. Zhao, Techno-economic and environmental assessment of a novel co-generation system integrating heat pump with Allam cycle, Energy Convers. Manag. 277 (2023) 116606, https://doi.org/10.1016/j.enconman.2022.116606.
[15] H. Yu, T. Gundersen, E. Gençer, Optimal liquified natural gas (LNG) cold energy utilization in an Allam cycle power plant with carbon capture and storage, Energy Convers. Manag. 228 (2021) 113725, https://doi.org/10.1016/j.enconman.2020.113725.
[16] L. Wang, S.M. Alirahmi, H. Yu, Development and analysis of a novel power-to-gas-to-power system driven by the Allam cycle for simultaneous electricity and water production, Energy Convers. Manag. 319 (2024) 118934, https://doi.org/10.1016/j.enconman.2024.118934.
[17] M. Xie, X. Chen, L. Chen, M. Zhou, Y. Liu, L. Zeng, H. Shi, F. Zhang, S. Xie, Y. Zhao, Evaluating the feasibility of a novel Allam cycle for co-generating power and water in hot regions, Energy Convers. Manag. 309 (2024) 118447, https://doi.org/10.1016/j.enconman.2024.118447.
[18] J. Luo, O. Emelogu, T. Morosuk, G. Tsatsaronis, Exergy-based investigation of a coal-fired allam cycle, Energy 218 (2021) 119471, https://doi.org/10.1016/j.energy.2020.119471.
[19] Y. Zhao, B. Wang, J. Chi, Y. Xiao, Parametric study of a direct-fired supercritical carbon dioxide power cycle coupled to coal gasification process, Energy Convers. Manag. 156 (2018) 733–745, https://doi.org/10.1016/j.enconman.2017.11.044.
[20] W. Chan, T. Morosuk, X. Li, H. Li, Allam cycle: Review of research and development, Energy Convers. Manag. 294 (2023) 117607, https://doi.org/10.1016/j.enconman.2023.117607.
[21] H. Li, J.P. Jakobsen, Ø. Wilhelmsen, J. Yan, PVTxy properties of CO2 mixtures relevant for CO2 capture, transport and storage: Review of available experimental data and theoretical models, Appl. Energy 88 (2011) 3567–3579, https://doi.org/10.1016/j.apenergy.2011.03.052.
[22] R. Span, W. Wagner, A new equation of state for carbon dioxide covering the fluid region from the triple-point temperature to 1100 K at pressures up to 800 MPa, J. Phys. Chem. Ref. Data 25 (1996) 1509–1596, https://doi.org/10.1063/1.555991.
[23] I. Tsivintzelis, G.M. Kontogeorgis, M.L. Michelsen, E.H. Stenby, Modeling phase equilibria for acid gas mixtures using the CPA equation of state. Part II: Binary mixtures with CO2, Fluid Phase Equilib. 306 (2011) 38–56, https://doi.org/10.1016/j.fluid.2011.02.006.
[24] S.A. Zaryab, R. Scaccabarozzi, E. Martelli, Advanced part-load control strategies for the Allam cycle, Appl. Therm. Eng. 168 (2020), https://doi.org/10.1016/j.applthermaleng.2019.114822.
[25] R. Allam, S. Martin, B. Forrest, J. Fetvedt, X. Lu, D. Freed, G.W. Brown, T. Sasaki, M. Itoh, J. Manning, Demonstration of the Allam Cycle: An update on the development status of a high efficiency supercritical carbon dioxide power process employing full carbon capture, Energy Procedia 114 (2017) 5948–5966, https://doi.org/10.1016/j.egypro.2017.03.1731.
[26] F. Okoro, A. Chapoy, P. Ahmadi, R. Burgass, Validation of cubic EoS mixing rules and multi-fluid helmholtz energy approximation EoS for the phase behaviour modelling of CO_2-rich binary mixtures at low temperatures, Greenhouse Gases Sci. Technol. 14 (2024) 829–858, https://doi.org/10.1002/ghg.2300.
[27] H. Li, J. Yan, J. Yan, M. Anheden, Impurity impacts on the purification process in oxy-fuel combustion based CO_2 capture and storage system, Appl. Energy 86 (2009) 202–213, https://doi.org/10.1016/j.apenergy.2008.05.006.
[28] M. Mazzoccoli, B. Bosio, E. Arato, Pressure-density-temperature measurements of binary mixtures rich in CO_2 for pipeline transportation in the CCS process, J. Chem. Eng. Data 57 (2012) 2774–2783, https://doi.org/10.1021/je300590v.
[29] W. Xiong, L.-H. Zhang, Y.-L. Zhao, S.-M. Wen, L.-L. Liu, Z.-L. Cao, Y.-C. Wang, S.-G. Luo, X.-Y. Jiang, Phase equilibrium modeling for CCUS fluids using a modified association equation of state, J. Supercrit. Fluids 219 (2025) 106543, https://doi.org/10.1016/j.supflu.2025.106543.
[30] M. Vitali, M. Leporini, O. Masi, A. Speranza, F. Corvaro, B. Marchetti, Net zero Flow Assurance - Validation of various equations of state for the prediction of VLE and density of CO_2-rich mixtures for CCUS applications, Int. J. Greenhouse Gas Control 125 (2023) 103877, https://doi.org/10.1016/j.ijggc.2023.103877.
[31] J. Gernert, R. Span, EOS-CG: A Helmholtz energy mixture model for humid gases and CCS mixtures, J. Chem. Thermodyn. 93 (2016) 274–293, https://doi.org/10.1016/j.jct.2015.05.015.
[32] H. Li, B. Dong, Z. Yu, J. Yan, K. Zhu, Thermo-physical properties of CO2 mixtures and their impacts on CO_2 capture, transport and storage: Progress since 2011, Appl. Energy 255 (2019), https://doi.org/10.1016/j.apenergy.2019.113789.
[33] T. Neumann, S. Herrig, I.H. Bell, R. Beckmüller, E.W. Lemmon, M. Thol, R. Span, EOS-CG-2021: A mixture model for the calculation of thermodynamic properties of CCS mixtures, Int. J. Thermophys. 44 (2023) 178, https://doi.org/10.1007/s10765-023-03263-6.
[34] C. McKay, M. Nazeri, H. Haghighi, D. Erickson, Recommendations for the selection of equation of state during design and operation of impure CO2 transport and storage, in: 16th International Conference on Greenhouse Gas Control Technologies, 2022.
[35] A. Rogalev, E. Grigoriev, V. Kindra, N. Rogalev, Thermodynamic optimization and equipment development for a high efficient fossil fuel power plant with zero emissions, J. Clean Prod. 236 (2019), https://doi.org/10.1016/j.jclepro.2019.07.067.
[36] K. Brun, P. Friedman, R. Dennis, Fundamentals and applications of supercritical carbon dioxide (sCO_2) based power cycles, Woodhead Publishing Series, Energy (2017).
[37] I. Velázquez F. Demeyer M. Reyes, Optimization of Equations of State for Supercritical CO2-Rich Mixtures and Their Impact on the Modeling of Carbon Capture & Storage Systems, 2024, https://doi.org/10.2139/ssrn.4999304.
[38] Aspen Plus | Leading Process Simulation Software | AspenTech, (n.d.). https://www.aspentech.com/en/products/engineering/aspen-plus (accessed June 12, 2023).
[39] E.W. Lemmon, I.H. Bell, M.L. Huber, M.O. McLinden, NIST Standard Reference Database 23: Reference Fluid Thermodynamic and Transport Properties-REFPROP, Version 10.0, National Institute of Standards and Technology, 2018.
[40] J.H. Horlock, D.T. Watson, T.V. Jones, Limitations on gas turbine performance imposed by large turbine cooling flows, J. Eng. Gas Turbine Power 123 (2001) 487–494, https://doi.org/10.1115/1.1373398.
[41] M.A. El-Masri, On thermodynamics of gas-turbine cycles: Part 2—a model for expansion in cooled turbines, J. Eng. Gas Turbine Power 108 (1986) 151–159, https://doi.org/10.1115/1.3239862.
[42] K. Wimmer, W. Sanz, Optimization and comparison of the two promising oxy-combustion cycles NET Power cycle and Graz Cycle, Int. J. Greenhouse Gas Control 99 (2020), https://doi.org/10.1016/j.ijggc.2020.103055.
[43] T. Xin, C. Xu, Y. Yang, V. Kindra, A. Rogalev, A new process splitting analytical method for the coal-based Allam cycle: Thermodynamic assessment and process integration, Energy 267 (2023) 126634, https://doi.org/10.1016/j.energy.2023.126634.
[44] Q. Zhao, M. Mecheri, T. Neveux, R. Privat, J.N. Jaubert, Selection of a proper equation of state for the modeling of a supercritical CO_2 Brayton cycle: Consequences on the process design, Ind. Eng. Chem. Res. 56 (2017) 6841–6853, https://doi.org/10.1021/acs.iecr.7b00917.
[45] O.E. Baljé,, A study on design criteria and matching of turbomachines: Part A—similarity relations and design criteria of turbines, J. Power Eng. Power 84 (1962) 83–102, https://doi.org/10.1115/1.3673386.
[46] O.E. Baljé,, A study on design criteria and matching of turbomachines: Part B—compressor and pump performance and matching of turbocomponents Journal of Engineering for, J. Power Eng. Power 84 (1962) 103–114, https://doi.org/10.1115/1.3673350.
[47] D. Fleming, T. Holschuh, T. Conboy, G. Rochau, R. Fuller, Scaling considerations for a multi-megawatt class supercritical co2 brayton cycle and path forward for commercialization, in: Manufacturing Materials and Metallurgy; Marine; Microturbines and Small Turbomachinery; Supercritical CO2 Power Cycles, American Society of Mechanical Engineers, vol. 5, 2012: pp. 953–960, https://doi.org/10.1115/GT2012-68484.
[48] Y. Du, C. Yang, H. Wang, C. Hu, One-dimensional optimisation design and off-design operation strategy of centrifugal compressor for supercritical carbon dioxide Brayton cycle, Appl. Therm. Eng. 196 (2021) 117318, https://doi.org/10.1016/j.applthermaleng.2021.117318.
[49] E.E. Didier, G.A. Perez, Short cut method for cost estimation in ditillation columns, Cost Eng. (2003).
[50] The MathWorks Inc, MATLAB version: 9.13.0 (R2022b), (2022). https://www.mathworks.com (accessed June 12, 2023).
[51] J. Andersson, Multiobjective optimization in engineering design : applications to fluid power systems, PhD dissertation, Linköpings universitet, Linköping, 2001., n.d.
[52] E. Martelli, E. Amaldi, PGS-COM: A hybrid method for constrained non-smooth black-box optimization problems, Comput. Chem. Eng. 63 (2014) 108–139, https://doi.org/10.1016/j.compchemeng.2013.12.014.
[53] M. Ibrahim, G. Skaugen, I.S. Ertesvåg, T. Haug-Warberg, Modelling CO2 - water mixture thermodynamics using various equations of state (EoSs) with emphasis on the potential of the SPUNG EoS, Chem. Eng. Sci. 113 (2014) 22–34, https://doi.org/10.1016/j.ces.2014.03.025.
[54] F. Okoro, A. Chapoy, P. Ahmadi, R. Burgass, Effects of non-condensable CCUS impurities (CH4, O2, Ar and N2) on the saturation properties (bubble points) of CO2 -rich binary systems at low temperatures (228.15–273.15 K), Greenhouse Gases Sci. Technol. 14 (2024) 62–94, https://doi.org/10.1002/ghg.2252.
[55] A. Seppo, Korpela, Principles of Turbomachinery, Second, John Wiley & Sons. Inc, The Ohio Sate, 2020.
[56] Y.H. Fan, G.H. Tang, X.L. Li, D.L. Yang, General and unique issues at multiple scales for supercritical carbon dioxide power system: A review on recent advances, Energy Convers. Manag. 268 (2022) 115993, https://doi.org/10.1016/j.enconman.2022.115993.
[57] J.S. Kwon, S. Son, J.Y. Heo, J.I. Lee, Compact heat exchangers for supercritical CO2 power cycle application, Energy Convers. Manag. 209 (2020) 112666, https://doi.org/10.1016/j.enconman.2020.112666.